CORE
Provided by Digital.CSIC
Metadata, citation and similar papers at core.ac.uk

Journal of The Electrochemical Society, 157 (7) H711-H720 (2010)
0013-4651/2010/157(7)/H711/10/$28.00 © The Electrochemical Society

Analysis of Excess Carrier Concentration Control in Fast-Recovery High Power Bipolar Diodes at Low Current Densities

X. Perpiñà,[a,z] X. Jordà,[a] M. Vellvehi,[a] J. Vobecky,[b] and N. Mestres[c]

[a]Instituto de Microelectrónica de Barcelona, IMB-CNM (CSIC), Campus Universitat de la Autònoma de Barcelona, Bellaterra, Barcelona 08193, Spain
[b]ABB Switzerland Limited, Semiconductors, CH-5600 Lenzburg, Switzerland
[c]Institut de Ciència dels Materials de Barcelona (ICMAB-CSIC), Campus Universitat de la Autònoma de Barcelona, Bellaterra, Barcelona 08193, Spain

The combination of emitter control with local lifetime tailoring by ion irradiation is experimentally analyzed in fast-recovery high power diodes. For this purpose, the carrier lifetime and excess carrier concentration profiles are measured and modeled within the low doped region of unirradiated and helium irradiated diodes under low current densities (<20 A/cm^2). The interest in working under these current conditions responds to the fact that the only recombination mechanism that modulates the steady-state carrier concentration is that of the multiphonon-assisted case (Shockley–Read–Hall model). This enables us to extract parameters for their modeling under arbitrary working conditions and to detect the influence of ion irradiation on the excess carrier distribution. For a better comprehension of the results, the excess carrier profile in the unirradiated diode is physically analyzed in detail by an analytical model. Afterward, physical simulations are also carried out, employing the experimental lifetime profiles as input parameters. As a result, a very good agreement between simulation predictions and experiments is observed, which is used to explain, by the support of analytical expressions, how the ion-irradiation process can improve the diode operation at low current densities during the late phase of the reverse recovery.
© 2010 The Electrochemical Society. [DOI: 10.1149/1.3421974] All rights reserved.

Manuscript received February 24, 2010. Published May 10, 2010.

The main difference between low and high power discrete bipolar diodes is the presence of a thick low N-doped layer (drift region) between highly P- and N-doped layers (emitters), which allows high power diodes reaching blocking voltages in the kilovolt range.

During the blocking state (off-state), the drift region is gradually depleted until the full bus voltage is sustained by the PN$^-$ junction. In an on-state, carriers are injected from the highly doped layers into the drift region, finally reaching an excess carrier concentration much higher than that of the doping level (high injection condition). Such a physical effect changes the initial resistivity of this layer (conductivity modulation), highly reducing the power losses during the on-state.

The transition from an on-state to an off-state (reverse recovery) requires a certain time (reverse recovery time) because the device drift region stores a large amount of excess carriers that should be removed. This removal time increases as the drift region is thicker. Additionally, it is required that for a safe reverse recovery process, the current flowing across the diode shows a smooth decay (soft behavior) without oscillations (snappy behavior), and the reverse current peak should be as small as possible.[1]

Nowadays, two strategies are basically used to improve the reverse recovery response of power diodes: the emitter[2] and lifetime engineering.[3] There also exist sophisticated methods that utilize special PNP structures at the cathode side, e.g., field charge extraction[4] or controlled injection of back-side holes)[5] diodes. However, their implementation is more complicated and not without compromises. The emitter and lifetime engineering are based on tailoring the excess carrier concentration profile in the drift region.[6] By using emitter engineering, the injection efficiency at the PN$^-$ junction is controlled by the doping level of a single diffused emitter (single diffused anode) or the insertion of a buffer layer with a lower doping level (double diffused anode) to increase the breakdown voltage at the same time, also implying in the second case a reduction of the device drift region. By contrast, lifetime engineering (or lifetime killing) relies on the possibility of adjusting the lifetime of the carriers injected into the drift region by inducing generation–recombination centers (deep level introduction within the energy bandgap).[7] They can be created by noble metal atoms (diffusion or postimplantation "drive-in" of platinum or gold at high temperatures), electron irradiation, or ion irradiation (protons or alpha particles). Lifetime tailoring is not recommendable in diodes with a single diffused anode as this process raises the power losses during the on- and off-states. This is not a problem when a double diffused anode is employed and the deep levels for the local lifetime killing are outside the space charge region.[8] Then, a convenient trade-off is obtained between the static and dynamic parameters of the device. As a matter of fact, both strategies, the lifetime and emitter engineering, are frequently combined, while one of them has a predominant role in the final characteristics of the device.[6]

Commonly, the previous study for an optimal ion irradiation is assisted by numerical simulations of the involved physical phenomena,[9-12] which require an accurate selection of their input parameters. Although deep level transient spectroscopy (DLTS) and *C-V* profiling may provide information about recombination centers' characteristics (energy levels and spatial distribution) appropriate for this purpose, the evolution of excess carrier concentration in the drift region of a biased device is not directly measured. Moreover, the measurements of the carrier lifetime profile with traditional methods, such as open-circuit voltage decay[13,14] (OCVD), do not have enough accuracy to spatially resolve such local effects due to ion irradiation. For this reason, OCVD measurements should be complemented with free-carrier absorption (FCA) results.[15,16] Previous works on this field were carried out by Rosling et al.[16] Using the FCA technique, they measured the excess carrier concentration profile in electron and proton irradiated PIN diodes nonoptimized for actual working applications. They neither analyzed in detail the underlying physics concerning the excess carrier injection into the diode drift region nor described the excess carrier local modulation. Other works have been carried out to perform the calibration of the Shockley–Read–Hall (SRH) model, but always in homogeneously lifetime tailored power devices.[17,18]

This work intends to perform FCA measurements with fast-recovery diodes irradiated with alpha particles (He^{2+}) and critically discusses their effects on the device behavior. Particularly, our study focuses on the determination of the excess carrier concentration behavior within unirradiated and irradiated diodes under low current density pulses (from 1 to 16 A/cm^2), extracting the steady-state excess carrier concentration and lifetime profiles within the drift region. From their comparison, it is possible to infer the differences in their physical behavior during the diode turn-off, as the steady-state excess carrier profile predetermines the course of the reverse

[z] E-mail: xavier.perpinya@imb-cnm.csic.es

Downloaded 11 May 2010 to 205.161.180.253. Redistribution subject to ECS license or copyright; see http://www.ecsdl.org/terms_use.jsp

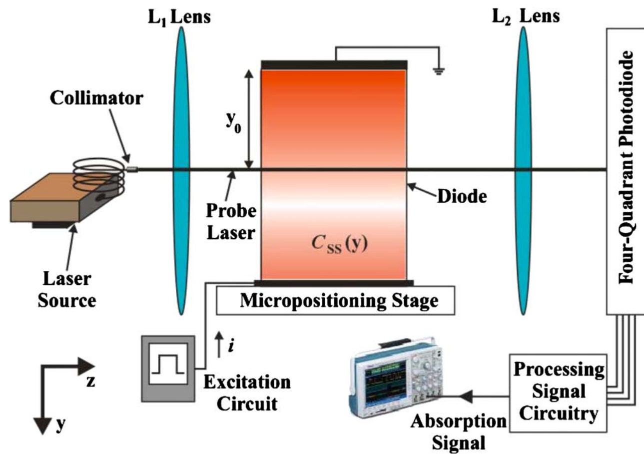

Figure 1. (Color online) Schematic of the setup when performing FCA measurements within the diode (not to scale).

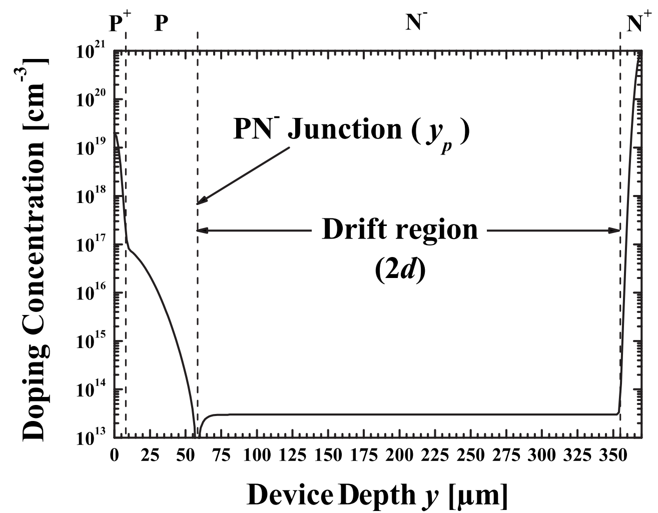

Figure 2. Internal structure of the studied devices.

recovery process.[1] The interest in working under these current densities responds to the fact that the recombination mechanism, which governs the steady-state excess carrier concentration profile, is the multiphonon-assisted or SRH model. This allows us to directly inspect the ion-irradiation effects on the SRH recombination, avoiding other recombination mechanisms that could shield them. Moreover, employing an analytical model, it is possible to assist in the interpretation of the obtained experimental results from the unirradiated device and to extract the lifetime profiles within both diodes to finally perform two-dimensional (2D) physical simulations. Finally, a very good agreement is observed between measurements and simulation.

Steady-State Excess Carrier Concentration and Lifetime Characterization

The excess carrier concentration profile and its corresponding lifetime have been measured by OCVD and FCA techniques. On the one hand, OCVD measurements permit extracting the carrier lifetime averaged within the drift region by an electrical measurement.[14,19] The diode works in the on-state under a resistive load with a small parasitic inductance in series. Suddenly, the current is rapidly cut by the action of a fast external semiconductor switch, leaving the diode in an open circuit and forcing the excess carrier removal by internal recombination and diffusion processes.[20] This is electrically manifested on the time decay of the diode voltage drop, in which two linear slopes that correspond to the conditions of high or low injection are observed. The former allows us to determine the high level lifetime τ_{HL} (carrier high injection), while the latter permits us to extract the low level lifetime τ_{LL} (carrier low injection), both as an average value inside the device. This magnitude can be determined from the slope of the voltage tail dV/dt using the following relationship[14]

$$\tau_m = \frac{-nk_BT/q}{dV/dt} \qquad [1]$$

where m and n make reference to the injection regime (m = LL and $n = 1$ in low injection; m = HL and $n = 2$ in high injection); k_B and T are the Boltzmann constant and temperature, respectively. One may rewrite both lifetimes in terms of the minority lifetime of electrons (τ_{n0}) and holes (τ_{p0}) as[21,22] $\tau_{HL} = \tau_{n0} + \tau_{p0}$ and $\tau_{LL} = \tau_{p0}$.

On the other hand, FCA measurements allow determining the excess carrier concentration inside the device when high injection conditions are reached in the inspected layer.[23] In this technique, an IR-laser probe beam ($\lambda = 1.3$ µm) passes through a biased diode under test (DUT) perpendicularly striking on its lateral sides or walls at a given depth y_0, as depicted in Fig. 1. When the DUT is turned on, carriers coming from the emitters are injected into the drift region, eventually establishing an excess carrier concentration C higher than that of the doping level (high injection condition). This effect modifies the semiconductor optical properties, enhancing the material absorption at the near-infrared spectrum due to the excess carrier presence. From the radiation absorption measurements, it is possible to deduce a longitudinal averaged value of C at a given depth y_0 from the top surface.[15] Additionally, if the excitation circuit is able to cut the diode bias current (I_{bias}) faster compared to the carriers' lifetime, a depth-resolved lifetime averaged along the interaction laser DUT is derived (open-circuit carrier decay).[24] Figure 1 also shows the main elements of the experimental rig: the laser source, two lenses for controlling the laser beam shape, the sensing setup (four-quadrant photodiode and processing signal circuitry), and the biasing circuit for the device electrical excitation. More details on this setup are given in Ref. 15 and 25. The excess carrier concentration C is extracted from the transmitted radiation power through the DUT by[15]

$$C = \frac{1}{L\left(\frac{\partial \alpha}{\partial C}\right)} Ln\left(\frac{V_{out,P}}{V_{out,P(t)}}\right) \qquad [2]$$

where L denotes the interaction length with the sample. $V_{out,P}$ and $V_{out,P(t)}$ represent the output signal of the radiation power sensed by the detector before and during the diode excitation, respectively. In this expression, it is considered that the absorption coefficients α and C are linearly related, $(\partial\alpha/\partial C)$ being the proportionality constant between them. At $\lambda = 1.3$ µm and in similar experimental conditions of this work, this coefficient was determined by Schlögl,[26] obtaining $(\partial\alpha/\partial C) = 8.08 \times 10^{-18}$ cm^{-2}.

Diode Structure and FCA Experimental Results

Diodes' description.— The studied devices are 100 A/2.5 kV circular power diodes (area 2 cm^2). Their total thickness is 390 µm, also considering top and bottom aluminum contacts (10 µm each one). As depicted in Fig. 2, their internal structure consists of a double diffused anode (P^+ and P-buffer), a wide drift region ($N^-, 2d = 297$ µm), and a single diffused cathode (N^+). The presence of the P-buffer layer was to achieve a high breakdown voltage and to slightly modulate the excess carrier concentration in the on-state, as previously stated. From the point of view of the FCA measurements, the drift region thickness allowed the excess carrier concentration measurement inside the device without having spatial restrictions imposed by the sample. Additionally, excess carrier measurements were feasible within the P-buffer layer, as its doping level

Downloaded 11 May 2010 to 205.161.180.253. Redistribution subject to ECS license or copyright; see http://www.ecsdl.org/terms_use.jsp

was lower than the excess carrier concentration reached during the on-state. This allowed detecting whether the high injection condition could be reached in this layer. The PN^- junction was located 58 μm from the anode top. The junction termination consisted of a positive bevel with surface passivation using a rubber. The helium irradiation was performed through the anode contact (10 μm thick aluminum) with a fluence of 10^{10} cm^2 and an energy of 11 MeV. This process located the defect peak in the range $r_p = 60–65$ μm. Afterward, all diodes were annealed at 200°C for 60 min to remove the unstable radiation defects. As a result, the carrier lifetime was altered close to the PN^- junction depth y_p. More details about the electrical behavior of these diodes can be found in Ref. 9.

Experimental conditions.— Concerning the sample preparation, the diodes were cut in strips of 1.5 × 10 mm, and afterward, their lateral walls were polished following physical and chemical processes.[27] Therefore, the spatial resolution and radiation power transmission were enhanced. After that, the strips were finally soldered and bonded on a power substrate (insulated metal substrate). This last step introduces a relatively high contact resistance on the measured samples because their standard mounting is in press pack housing, supporting pressures up to 100 kN/cm^2. However, depending on the chosen biasing conditions (below 30 A/cm^2), this parasitic resistance would not excessively influence the real distribution of excess carrier concentration inside the device also because there is no current flowing through the contacts during OCVD measurements. The device was biased with short current pulses at low density values using a high speed insulated gate bipolar transistor (IGBT) (IXGH22N50BS). The IGBT was connected in series with a resistive load, a parasitic inductance, and the DUT. Switching on and off the IGBT, the diode was forward biased with current pulses up to 16 A/cm^2 for 84 μs. Thus, device self-heating effects were avoided, as well as contact self-heating problems or current instabilities due to the high contact resistance. Additionally, the other recombination processes, i.e., Auger and radiative recombinations, were not manifested in the selected current range, as they appeared at higher current densities (>50 and >100 A/cm^2, respectively).[23,28-30]

Influence of diode preparation process on experimental results.— SRH recombination processes can be produced either inside the bulk or at any surface/interface defined between silicon and another material (e.g., chip lateral walls). The excess carriers' lifetime measured by OCVD and FCA provides a carrier effective lifetime $\tau_{m,\text{eff}}$ depending on $\tau_{m,\text{bulk}}$ (bulk lifetime) and $\tau_{m,\text{surf}}$ (surface lifetime) as

$$\frac{1}{\tau_{m,\text{eff}}} = \frac{1}{\tau_{m,\text{bulk}}} + \frac{1}{\tau_{m,\text{surf}}} \quad [3]$$

where m makes reference to the injection regime reached within the drift region far from the lateral walls of the device or bulk (m = LL in low injection; m = HL in high injection). From the point of view of the device physical modeling, the $\tau_{m,\text{bulk}}$ profile is more interesting as an input simulation parameter than the $\tau_{m,\text{surf}}$ because $\tau_{m,\text{bulk}}$ determines the excess carrier profiles in a real working diode. However, the DUT preparation process (cutting and polishing the diode) changes the initial $\tau_{m,\text{surf}}$, and its contribution to $\tau_{m,\text{eff}}$ cannot be neglected (specially when m = HL). This fact makes the $\tau_{m,\text{bulk}}$ determination from $\tau_{m,\text{eff}}$ more difficult.

To qualitatively evaluate and stress the influence of the surface recombination on the measured excess carrier profile in steady state (C_{SS}) and its effective lifetime profile, physical simulations with Sentaurus device TCAD [31] were performed. The simulated structure corresponds to a half cross section of the diode strip forward biased under a current density of 8 A/cm^2 for both cases (irradiated and unirradiated diodes), where the interface defined between air and silicon at one of the lateral walls is also assumed. In contrast to the bulk SRH theory, the parameter that accounts for this effect in the surface SRH model is the surface recombination velocity (S_{SRH}).

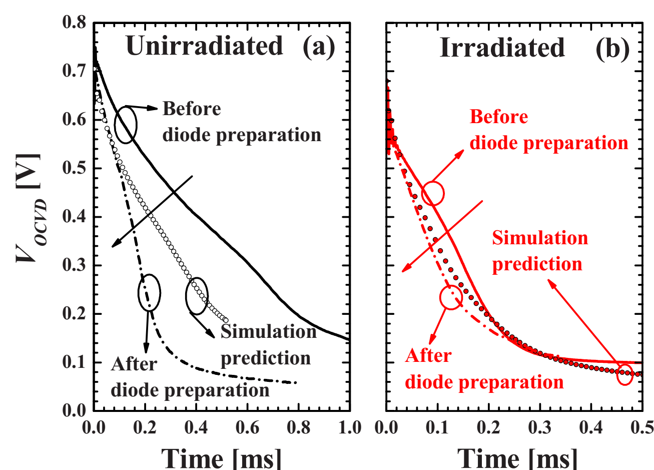

Figure 3. (Color online) OCVD measurements and simulated results, evidencing the influence of diode preparation on the excess carriers' lifetime.

The S_{SRH} measurement is very difficult, as S_{SRH} and $\tau_{m,\text{surf}}$ follow a transcendental equation.[32,33] S_{SRH} measurements were only carried out on the top and bottom surfaces of silicon wafers[33,34] or at the oxide interface of ultrathin silicon-on-insulator wafers.[35] For this reason, the parameter determination for each case was faced differently. τ_{n0} and τ_{p0} were directly measured on the unirradiated diode by OCVD ($\tau_{n0} = 63$ and $\tau_{p0} = 31$ μs), and S_{SRH} was extracted from the literature ($S_{SRH} = 2800$ cm/s reported in Ref. 34). Concretely, $S_{SRH} = 2800$ cm/s was measured on silicon wafers with polished surfaces,[34] and similar values were estimated on laterally polished diodes in Ref. 29. In the irradiated device, all defects created by the irradiation were taken into account, and their profiles were determined by SRIM simulations.[11,36]

Figure 3a and b compares the typical OCVD measurements for each diode (before and after the diode preparation process) with simulation results considering only the surface recombination at the lateral walls of the sample. It is observed from the OCVD measurements that the lifetime was extremely reduced due to the preparation process in both cases, obtaining a good agreement with simulation results. $\tau_{\text{HL,bulk}}$ and $\tau_{\text{HL,eff}}$ were determined from the OCVD measurements performed before and after the diode preparation. By using Eq. 3, $\tau_{\text{HL,surf}}$ can also be derived. $\tau_{\text{HL,surf}}$ are 16 and 25 μs for the unirradiated and irradiated diodes, respectively. One may expect from the similarity of these values that they are related to the preparation process (cutting–polishing). As this process generates a certain amount of defect density on the sample lateral walls in an unrepeatable way, $\tau_{\text{HL,surf}}$ is considered as a stochastic error source on the $\tau_{\text{HL,bulk}}$ determination. Another result from OCVD measurements is that no dependence of the measured $\tau_{\text{HL,eff}}$ on the current i has been obtained, which means that $\tau_{\text{HL,eff}}$ is not a function of excess carrier at the current levels considered in this work. Moreover, the recombination at the end regions (emitters, i.e., P-buffer and N^+-layers) did not affect the results because the OCVD lifetime was calculated when the charge in the emitters was removed.[14] The fact that there is no current flow through the contacts out of the device is one of the biggest advantages of the OCVD method: Lifetime is not influenced by contacts and very little by emitters.

Figure 4 demonstrates how the surface recombination modulates the excess carrier distribution inside the device. Figure 4a and b contains both the 2D and one-dimensional (1D) cuts of electron concentration in steady state (both the doping level and excess carriers, C_n) normalized to its highest value achieved close to the PN^- junction ($C_{n,\max}$). Only C_n is discussed here because both electrons and holes have the same concentration in the inspected region (high injection condition). Figure 4a visually shows how at 600 μm from the polished lateral wall, the $C_n/C_{n,\max}$ profile in the drift region

Downloaded 11 May 2010 to 205.161.180.253. Redistribution subject to ECS license or copyright; see http://www.ecsdl.org/terms_use.jsp

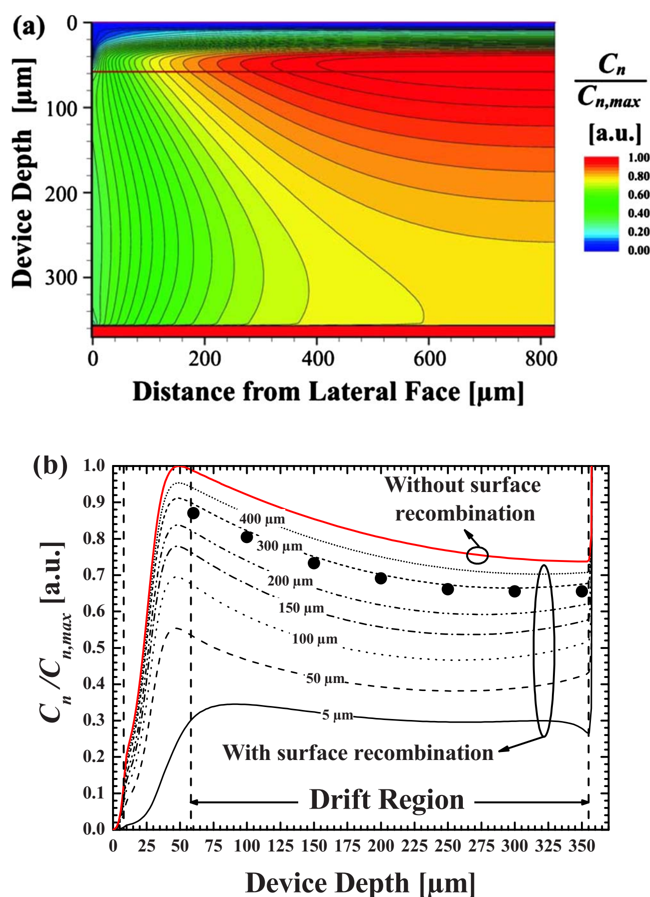

Figure 4. (Color online) (a) 2D electron density inside the simulated unirradiated diode where a surface recombination velocity of 2800 cm/s is considered. (b) Comparison of 1D vertical profiles of electron concentration obtained from considering (black lines) and not considering (red line) recombination at lateral walls, as well as the average of the electron concentration along the interaction length (black dot points).

experiences a transition from a 1D vertical profile to a 2D distribution, gradually decreasing until it reaches a constant value of 30% at the lateral wall. This effect is evident in Fig. 4b, where the consequences of assuming the surface recombination are depicted. In this figure, various vertical cuts of $C_n/C_{n,max}$ ranging from the lateral wall of 5 to 400 µm (black lines) are compared with the simulation results only considering bulk recombination (red line). From the simulation results in which surface recombination was taken into account, C_n profiles at several depths inside the drift region were averaged along the half interaction length (in the figure, distance from the lateral wall) to estimate the influence of the surface recombination on the measurements. After normalizing them to $C_{n,max}$ (black dot points), they are also represented in Fig. 4b. Only a deviation of 14% from simulation results without considering surface effects was obtained. Thus, because the consideration of such effect in the polished lateral walls did not excessively modify the simulation results, only bulk recombination was assumed in all performed simulations.

Time evolution of excess carrier concentration measured by FCA.— Figure 5a and b presents the evolution of the C profile for the irradiated and unirradiated cases when the diodes are excited with a current pulse (current density level of 5 A/cm^2), respectively. From these graphs, it is evident in both cases that C increases with time until reaching its steady-state value. In steady state, the irradiated diode has a lower concentration of excess carrier closer to the ion-irradiation range and shows an increase in C of 50% along

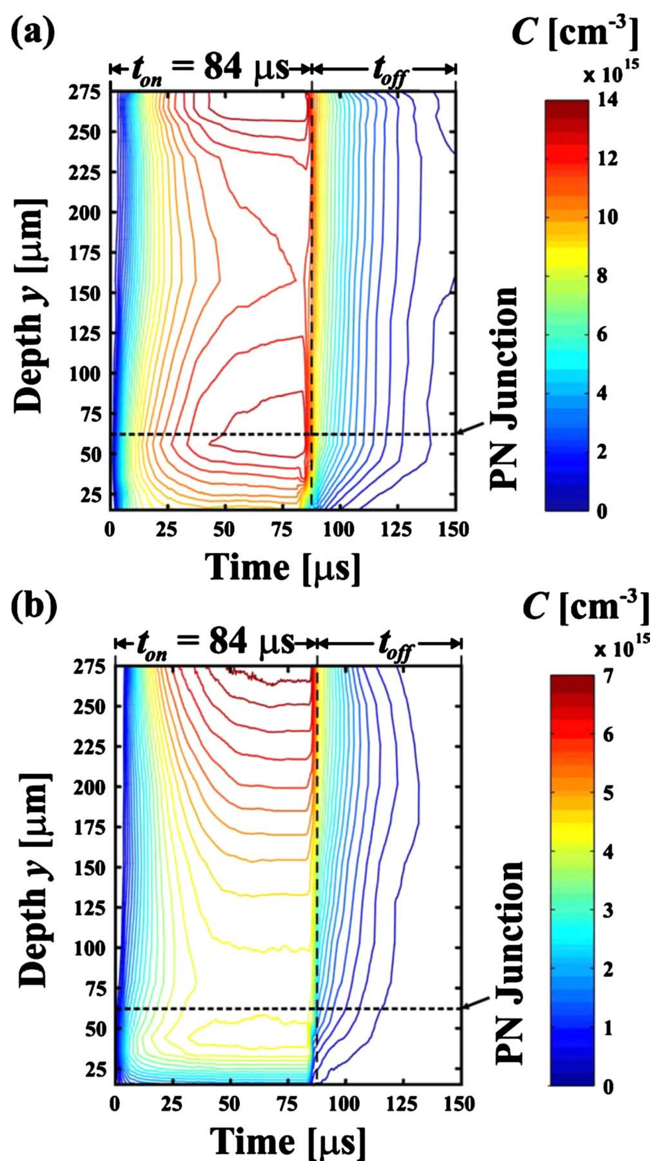

Figure 5. (Color online) Typical time evolution of excess carrier concentration at various depths inside the device (y) for (a) irradiated and (b) unirradiated diodes when a current pulse (5 A/cm^2) flows through them.

the device drift region. On the contrary, the unirradiated diode shows higher C values with a more homogeneous distribution along the drift region. At the end of the current pulse, the behavior of C during the diode turn-off is also observed depicting the excess carrier decay by diffusion and recombination. As evidenced in Fig. 5, the devices depict different decay times: The unirradiated diode shows a homogeneous carrier decay, whereas the other one exhibits a faster decay time close to the irradiated depth. For further insight into these behavioral differences, the measured profiles of decay time (which corresponds to $\tau_{HL,eff}$) and C_{SS} within the drift region are analyzed in the next sections, also comparing C_{SS} measurements with simulation results.

Depth-Resolved High Level Lifetime Extraction and Analysis

Ion-irradiation local effects on bulk high level lifetime profile.— The deep levels before irradiation (background high level lifetime, $\tau^{unir}_{HL,bulk}$) are described by a single level within the energy bandgap, whereas the radiation defects are represented by v inde-

Downloaded 11 May 2010 to 205.161.180.253. Redistribution subject to ECS license or copyright; see http://www.ecsdl.org/terms_use.jsp

Table I. Measured lifetimes through OCVD and FCA, jointly with the extracted $\tau_{HL,surf}$. In OCVD measurements, the error is not computed.

	Unirradiated	Irradiated
τ_0 (μs) from OCVD measurements previous to sample preparation	94	23
$\tau_{HL,eff}$ (μs) from OCVD measurements after sample preparation	20	16
$\tau_{HL,eff}$ (μs) from FCA measurements (drift region average far from irradiation depth)	19 ± 1	14 ± 1
$\tau_{HL,surf}$ calculated (μs)	16	24

pendent energy levels (no interaction among them).[37] Thus, the high level lifetime after irradiation $\tau_{HL,bulk}^{ir}$ is approximated by[38]

$$\frac{1}{\tau_{HL,bulk}^{ir}} = \frac{1}{\tau_{HL,bulk}^{unir}} + \sum_{i=1}^{v} \frac{1}{\tau_{a,i}} \quad [4]$$

where $\tau_{HL,bulk}^{unir}$ and $\tau_{a,i}$ represent the contributions of the deep levels before and after the irradiation to $\tau_{HL,bulk}^{ir}$, respectively. $\tau_{HL,bulk}^{unir}$ depends on the doping level N. This effect is usually accounted for by the empirical Scharfetter relation[38,39] that applies separately for the minority lifetimes of electrons and holes. When the diode is in on-state and its drift region is under high injection conditions, $\tau_{HL,bulk}^{unir}$ may be written as

$$\tau_{HL,bulk}^{unir} = \tau_0\left(a + \frac{b}{1 + \left(\frac{N}{N_{ref}}\right)^{\delta}}\right) \quad [5]$$

where τ_0 is the high level lifetime at the low doped regions (drift region), defined as the sum of the minority lifetimes of electrons and holes before the irradiation (i.e., $\tau_0 = 94$ μs). a, b, N_{ref}, and δ are fitting parameters with the same value for electrons and holes. a and b vary between 0 and 1 and verify the condition $a + b = 1$. N_{ref} and δ provide the lifetime decrease when the doping level increases, where $\delta = 1$ in silicon.[39]

Apart from the energy level introduced by the background deep levels, the irradiated devices can be modeled by only considering two other dominant energy levels[9,37] within the bandgap (i.e., $v = 2$): the vacancy–oxygen pair $VO^{(-/0)}$ ($E_C - 0.16$ eV, denoted as E1) and the single acceptor level of divacancy $V_2^{(-/0)}$ ($E_C - 0.42$ eV, denoted as E4). The former dominates the lifetime under high injection, whereas the latter is deeper within the bandgap and thus dominates the lifetime under low injection conditions[40,41] as long as the postirradiation annealing is not performed above 300°C. The deep levels resulting from the irradiation can contribute in a unique τ_{ir}, as can be inferred from Eq. 4. Therefore, the ion irradiation creates an inverse lifetime distribution $G(y)$ within the device as[42]

$$G(y) = \tau_{ir}^{-1} f(y) \quad [6]$$

where $f(y)$ corresponds to the normalized profile of defects induced by irradiation and is proportional to the loss of ion energy due to the interaction with the electrons and atoms. Mostly, all ion energy is dissipated close to the penetration range where the ions are finally stopped. $f(y)$ may be represented by the following equation[43]

$$f(y) = \begin{cases} \exp\left\{\frac{-[y - r_p(E)]^2}{2[\Delta r_p(E)]^2}\right\} & \text{if } y' < y \text{ (nuclear stopping)} \\ \exp\left\{\frac{-[y - r_p(E)]}{l}\right\} & \text{if } 0 \le y \le y' \text{ (electronic stopping)} \end{cases} \quad [7]$$

where $r_p(E)$ is the range (penetration depth) as a function of the incident ion energy, $\Delta r_p(E)$ represents the standard deviation of the ranges of individual particles (straggle), l is the defects' decay length defined from the ion range, and y' is the depth from which $f(y)$ makes the transition from the nuclear stopping behavior to the electronic one (defect tail).

Usually, the helium irradiation process is followed by annealing to remove the defects unstable at the working temperature range of the device, which would otherwise change the device parameters during its operation.[43] Therefore, from Eq. 4, the resulting $\tau_{HL,bulk}^{ir}$ when the diode is in the on-state and its drift region is under high injection corresponds to

$$\tau_{HL,bulk}^{ir}(y) = \tau_0\gamma(N)\left(\frac{1}{1 + \frac{\tau_0}{\tau_{ir}}\gamma(N)f(y)}\right) \quad [8]$$

where

$$\gamma(N) = \left(a + \frac{b}{1 + \left(\frac{N}{N_{ref}}\right)}\right)$$

Notice that τ_0^{-1} and τ_{ir}^{-1} are related to the density of the recombination centers $N_{t,0}$ (background) and $N_{t,i}$ (radiation induced for each energy level i) by the proportionality factors c_0 and c_i as $\tau_0^{-1} = (c_0 \times N_{t,0})$ and $\tau_{ir}^{-1} = \sum_{i=1}^{2}(c_i \times N_{t,i})$. c_0 and c_i are functions of the excess carrier concentration, the emission rate of carriers, and the capture rate of carriers (capture coefficients).[44]

Depth-resolved high level lifetime determination.— $\tau_{HL,eff}$ has been derived by fitting procedures on the carrier decay after turning off the current. The error in $\tau_{HL,eff}$ is evaluated from the fitting and considering the standard deviation of $\tau_{HL,eff}$ ($\sigma_{\tau_{HL,eff}}$) along the drift region, which is assumed as a stochastic noise introduced by a nonuniform surface carrier recombination. The spatial error in $\tau_{HL,eff}$ is mostly associated with the beam radius averaged along the interaction length with the diode (±12.5 μm). $\tau_{HL,surf}$ has been derived from FCA and OCVD results following the procedure previously mentioned: Before cutting the diode, the OCVD measurements are performed, and after the diode preparation, both the OCVD and FCA measurements are again carried out to quantify the lifetime variation. Table I reports these OCVD results before and after the diode preparation, jointly with the FCA lifetime measurements and the finally extracted $\tau_{HL,surf}$ for each device. Notice that in cut diodes, $\tau_{HL,eff}$ measured by OCVD agrees with the FCA results when they are averaged along the drift region.

For the determination of $\tau_{HL,bulk}$ in both cases, Eq. 3, 5, and 8 have been used. In the first place, the parameters a, b, and N_{ref} have been extracted by fitting Eq. 5 to the results of the unirradiated device, considering for τ_0 and $\tau_{HL,surf}$ the values detailed in Table I. The value obtained for N_{ref} agrees with other results reported (e.g., see Ref. 39). Once the parameters for the unirradiated case have been identified, the parameters $\Delta r_p(E)$, l, $r_p(E)$, and τ_{ir}^{-1} corresponding to $G(y)$ are determined by fitting Eq. 8 to $\tau_{HL,eff}$. Determining $G(y)$ is very interesting because it can be settled into any physical simulation package by introducing the extracted $f(y)$ and setting the simulation parameters to obtain the derived τ_{ir}^{-1}. All parameters resulting from these fittings are summarized in Table II.

Figure 6a and b compares $\tau_{HL,eff}$ and $\tau_{HL,bulk}$ between both diodes (the origin of the depth y is at the device top), respectively. The results obtained from the fitting of Eq. 5 and 8 are plotted within the range in which the high injection condition is reached (FCA measurement range). Figure 6a shows that the main difference between

Downloaded 11 May 2010 to 205.161.180.253. Redistribution subject to ECS license or copyright; see http://www.ecsdl.org/terms_use.jsp

Table II. Parameters extracted from fitting Eq. 8 to experimental results.

a	0.05
b	0.95
N_{ref} (cm^{-3})	7×10^{15}
τ_{ir}^{-1} (μs^{-1})	0.8
$r_p(E)$ (μm)	60
$\Delta r_p(E)$ (μm)	12
l (μm)	6

the measured results from the unirradiated and irradiated devices is the sudden increase in $\tau_{HL,eff}$ from 2.5 to 14 μs, experienced close to the ion-penetration range $r_p(E)$ (near the PN$^-$ junction) for the irradiated diode (red dot points), which contrasts with the constant profile (around 19 μs) obtained in the other case (black square points). This fact gives evidence for the local lifetime change, as previously noticed, and allows a direct inspection of the irradiation effects inside the diode. The difference observed between the measured values of $\tau_{HL,eff}$ for each device (i.e., 14 and 19 μs) is due to the sample preparation procedure because the surface recombination is not totally controlled during this process (see Table I), as previously stated. In Fig. 6a, experiments are compared to the theoretical predictions from Eq. 3 and 5-18 (unirradiated, in solid black line; irradiated, in dash red line).

Figure 6b shows the $\tau_{HL,bulk}$ extracted from Eq. 8 for the unirradiated and irradiated devices (in solid black and dash red lines, respectively). From the results, it is observed that the irradiation peak diminishes the lifetime locally at $r_p(E)$, and the defect tail has

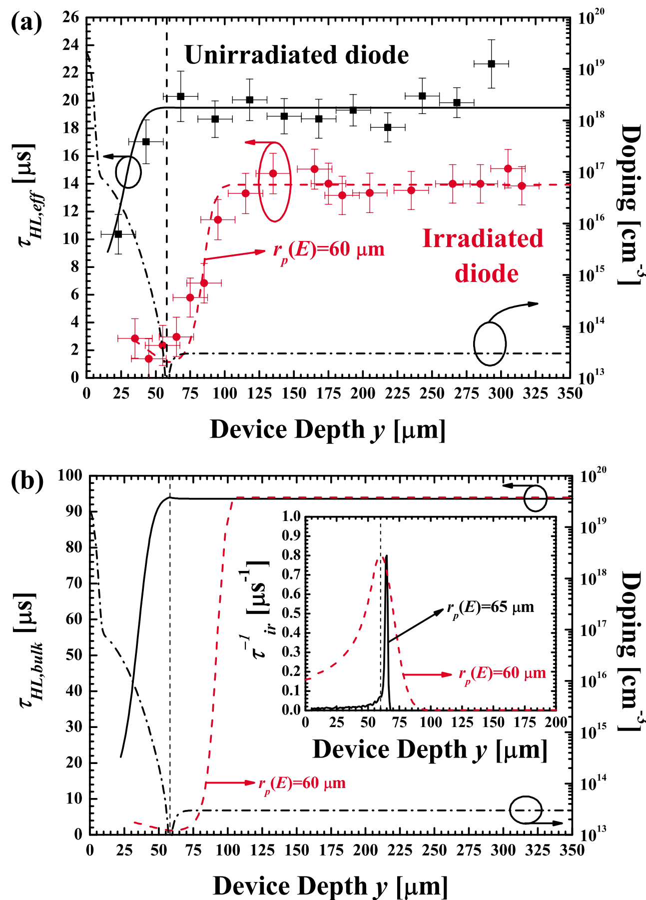

Figure 6. (Color online) Comparison of (a) $\tau_{HL,eff}$ and (b) $\tau_{HL,bulk}$ between both considered diodes (black square points, unirradiated; red dot points, irradiated).

a slight effect on the lifetime. The inset in Fig. 6b compares a defect profile derived from SRIM simulations[36] (solid black) to the results inferred from Eq. 8 (dash red). To better compare both curves, the curve in the inset that refers to SRIM simulations corresponds to the product of $f(y)$ derived from SRIM calculations with τ_{ir}^{-1} obtained from the fittings. The inset in Fig. 6b evidences how the fitting results present a higher $\Delta r_p(E)$ than SRIM simulations because the defects' diffusion during the irradiation and the subsequent thermal annealing are not taken into account by SRIM.[43,45] Moreover, SRIM results predict $r_p(E) = 65$ μm, in agreement with DLTS measurements shown in Ref. 46 with another diode, whereas the best fit of Eq. 8 is obtained when $r_p = 60$ μm (see Fig. 6a). This difference is in the error range when several devices are altogether irradiated in the same process (below 10 μm), as shown in Ref. 46. These results suggest that the procedure detailed above is suitable to experimentally extract $f(y)$.

Steady-State Excess Carrier Profile Analysis

Excess carrier concentration in unirradiated bipolar power diodes in steady state.— Under the current densities (i) at which bipolar power diodes are usually working, the excess carrier concentration of electrons (Δn) and holes (Δp) in the drift region is higher than that of the doping level N, verifying $\Delta n = \Delta p = C_{SS}$ (high injection condition). According to Ref. 47, the excess carrier concentration $C_{SS}(y)$ within the drift region for low current densities (<20 A/cm^2) depends on the depth y as

$$C_{SS}(y) = i\eta_m \frac{\tau_0}{q2L_a}\left\{\frac{\cosh[(y - y_p - d)/L_a]}{\sinh(d/L_a)} - B'\frac{\sinh[(y - y_p - d)/L_a]}{\cosh(d/L_a)}\right\} \quad [9]$$

where the origin is taken from the top of the P$^+$ anode layer (see Fig. 2), y_p corresponds to the location of the PN$^-$ junction, d represents a half of the drift region thickness, q is the electron charge, and L_a is the ambipolar diffusion length defined as $L_a = \sqrt{\tau_0 D_a}$ (D_a is the ambipolar diffusivity). The constant B' is defined as

$$B' = \frac{B + \eta_r - \eta_l}{\eta_m} \quad [10]$$

where B is expressed in terms of the electron and hole mobilities (μ_n and μ_p, respectively) as

$$B = \frac{\mu_n/\mu_p - 1}{\mu_n/\mu_p + 1} \quad [11]$$

and η_r, η_l, and η_m account for the contribution to the total current density corresponding, respectively, to the diffusion currents at the PN$^-$ [$i_n(y_p)$, electrons] and N$^-$N$^+$ [$i_p(y_p + 2d)$ holes] junctions and the excess carrier recombination within the drift region (i_m). All these coefficients must verify the condition

$$\eta_m + \eta_r + \eta_l = 1 \quad [12]$$

because the sum of all these current components must be equal to the total current i, that is

$$i = i_n(y_p) + i_m + i_p(y_p + 2d) \quad [13]$$

In turn, $i_n(y_p)$, $i_p(y_p + 2d)$, and i_m can be expressed as[47]

$$i_n(y_p) = \eta_l i = q\frac{D_n}{L_n}\coth\left(\frac{d_p}{L_n}\right)\frac{C_{SS}^2(y_p)}{N_A^-} \quad [14]$$

$$i_p(y_p + 2d) = \eta_r i = q\frac{D_p}{L_p}\coth\left(\frac{d_n}{L_p}\right)\frac{C_{SS}^2(y_p + 2d)}{N_D^+} \quad [15]$$

Downloaded 11 May 2010 to 205.161.180.253. Redistribution subject to ECS license or copyright; see http://www.ecsdl.org/terms_use.jsp

$$i_{\mathrm{m}} = \eta_{\mathrm{m}} i = \frac{q 2 d \bar{C}_{\mathrm{SS}}}{\tau} \quad [16]$$

where $\bar{C}_{\mathrm{SS}} = (1/2d)\int_{y_{\mathrm{p}}+2d}^{y_{\mathrm{p}}} dy C_{\mathrm{SS}}(y)$, N_{A}^{-} and N_{D}^{+} are the peak doping concentrations of the P-buffer and N^{+}-layers, d_{p} and d_{n} correspond to the thickness of the P-buffer and N^{+}-layers, D_{n} and L_{n} depict the electrons' diffusivity and diffusion length in the P-buffer layer, and D_{p} and L_{p} show the holes' diffusivity and diffusion length in the N^{+}-layer. This model predicts the displacement of the minima of the excess carrier concentration as a function of the emitter carriers' injection (see Eq. 10). This is an interesting issue as shown further on.

When designing a fast-reverse recovery diode, the following parameter is defined[1]

$$k = \frac{C_{\mathrm{SS}}(y_{\mathrm{p}})}{C_{\mathrm{SS}}(y_{\mathrm{p}} + 2d)} \quad [17]$$

which corresponds to the ratio between the excess carrier concentration at the PN^{-} and $N^{-}N^{+}$ junctions. Usually, for an optimum and reliable reverse recovery,[1] $k < 1$ is desired, i.e., $C_{\mathrm{SS}}(y_{\mathrm{p}}) < C_{\mathrm{SS}}(y_{\mathrm{p}} + 2d)$. With this excess carrier shape, the time required for the carrier removal close to the PN^{-} junction is shorter. Consequently, the depletion of the drift region to gradually sustain the blocking voltage is started earlier in time, hereby considerably reducing the peak reverse recovery current.[42] This unbalance is always obtained by emitter engineering or lifetime control processes, as can be seen from rewriting k in terms of technological parameters using Eq. 14 and 15 as follows

$$k = \sqrt{\frac{N_{\mathrm{A}}^{-}\eta_{\mathrm{l}}(D_{\mathrm{p}}/L_{\mathrm{p}})\coth(d_{\mathrm{n}}/L_{\mathrm{p}})}{N_{\mathrm{D}}^{+}\eta_{\mathrm{r}}(D_{\mathrm{n}}/L_{\mathrm{n}})\coth(d_{\mathrm{p}}/L_{\mathrm{n}})}} \quad [18]$$

From Eq. 18, it can be inferred that $C_{\mathrm{SS}}(y_{\mathrm{p}})$ can be diminished by either increasing d_{p} and diminishing $N_{\mathrm{A}}^{-}/N_{\mathrm{D}}^{+}$ (emitter-control, front-end process), or lowering L_{p}, L_{n}, and η_{l} (axial lifetime control techniques, back-end process).

Measured excess carrier concentration modulation by emitter control.— To demonstrate the influence of the P-buffer layer on the excess carrier concentration, the unirradiated device has been electrically excited by short current pulses (84 μs) from 1.5 to 16 A/cm^2. Subsequently, the model outlined in Eq. 9-12 has been employed for the sake of the results' interpretation by fitting it to the experimental data. To compute the carrier mobilities in Eq. 11, the following expression is used[42]

$$\mu_{\mathrm{n(p)}}^{-1} = \mu_{\mathrm{n(p)},0}^{-1} + 1/2\mu_{\mathrm{eh}}^{-1} \quad [19]$$

where $\mu_{\mathrm{p},0}$ and $\mu_{\mathrm{n},0}$ are the hole and electron mobilities when no temperature and injection effects are considered, and the term μ_{eh} takes into account the mobility reduction due to the e^{-}–h^{+} scattering. In this work, μ_{eh} has been described by the Cornwell–Weisskopf model[42]

$$\mu_{\mathrm{eh}}^{-1} = \frac{C_{\mathrm{SS}}(y)}{D} Ln[1 + F C_{\mathrm{SS}}^{-2/3}(y)] \quad [20]$$

where D and F are fitting parameters. To determine D_{a} and L_{a} in Eq. 9, the ambipolar mobility μ_{a} is calculated according to[42]

$$\mu_{\mathrm{a}}^{-1} = \mu_{\mathrm{p},0}^{-1} + \mu_{\mathrm{n},0}^{-1} + \mu_{\mathrm{eh}}^{-1} \quad [21]$$

This result allows the determination of the ambipolar diffusivity D_{a} under a high injection condition[42]

$$D_{\mathrm{a}} = \frac{2kT}{q}\mu_{\mathrm{a}} \quad [22]$$

All values of the parameters used in the computation of Eq. 19 and 22 are summarized in Table III.[48-50] D and F have been identified from fitting Eq. 20 to the measured ambipolar diffusion data reported in Ref. 50, obtaining $F = 2.14 \times 10^{12}$ and $D = 2.99 \times 10^{20}$ cm^{-1} V^{-1} s^{-1}. Furthermore, $C_{\mathrm{SS}}(y) \approx \bar{C}_{\mathrm{SS}}$ is assumed in Eq. 20. This is a good approximation because no significant variation in the measured $C_{\mathrm{SS}}(y)$ has been observed, and the model prediction agrees with the experimental data.

Table III. Parameters used for the mobility computation

	Value	Reference
$\mu_{\mathrm{n},0}$ (cm^2 V^{-1} s^{-1})	1360	48
$\mu_{\mathrm{p},0}$ (cm^2 V^{-1} s^{-1})	495	49
F (cm^{-2})	2.1372×10^{12}	This work and Ref. 50
D (cm^{-1} V^{-1} s^{-1})	2.9934×10^{20}	This work and Ref. 50

The fitting procedure consisted in introducing all known parameters into Eq. 9 and gradually determining $\eta_{\mathrm{m}}, \eta_{\mathrm{l}}, \eta_{\mathrm{r}}$, following an iteration loop and taking into account the relationship $\eta_{\mathrm{m}} + \eta_{\mathrm{l}} + \eta_{\mathrm{r}} = 1$. First, η_m was identified because it was the only parameter not directly measured, which provided the $\bar{C}_{\mathrm{SS}}$ value. After that, B' was extracted for each i. From the evaluation of B, η_l and η_r were determined using Eq. 10 and 12. This process was repeated until the error between the experimental points and the model prediction was minimized.

Figure 7a and b gives evidence for the emitter-control effects on C_{SS} when the current density i is increased. Figure 7a compares the C_{SS} model fit with the measured excess carrier data, showing a high agreement between experiment and theory. This figure also depicts that C_{SS} grows with increasing i (as the SRH model predicts) up to 11 A/cm^2, maintaining $k \sim 1$ approximately. From $i = 16$ A/cm^2, it is clearly observed as $k < 1$. Figure 7b depicts the dependence of the total current i on $C_{\mathrm{SS}}(y_{\mathrm{p}})$ and $C_{\mathrm{SS}}(y_{\mathrm{p}} + 2d)$. From Eq. 13-15, one may infer that i should quadratically depend on $C_{\mathrm{SS}}(y_{\mathrm{p}})$ and $C_{\mathrm{SS}}(y_{\mathrm{p}} + 2d)$, but in our measurements, there is a contribution of the recombination current in the drift region. This is inferred from the fact that although in both cases of $C_{\mathrm{SS}}(y_{\mathrm{p}})$ and $C_{\mathrm{SS}}(y_{\mathrm{p}} + 2d)$, a powerlike dependence has been measured, it is not a pure quadratic one. This behavior can be attributed to the low current biasing conditions (i_{m} contribution to i not negligible), as already observed in Ref. 51. Therefore, one may admit that there is a transition between a conduction current based on carrier recombination to another based on carrier diffusion at the PN^{-} and $N^{-}N^{+}$ junctions. One important outcome of the used model in Fig. 7a is that it allows extracting the dependence of η_{m}, η_{l}, and η_{r} on i, as well as the injection efficiency of the junctions $(\gamma_{\mathrm{l}}, \gamma_{\mathrm{r}})$ defined as follows[47]

$$\gamma_{\mathrm{l}} = (1 - \eta_{\mathrm{l}}) \quad [23]$$

$$\gamma_{\mathrm{r}} = (1 - \eta_{\mathrm{r}}) \quad [24]$$

$\gamma_{\mathrm{l}}(\gamma_{\mathrm{r}})$ provides information on the efficiency of a P (N) emitter when injecting holes (electrons) into the N^{-} drift region. In this process, the recombination at the P- and N^{+}-layers has been neglected because this effect is mostly manifested at higher i and C_{SS} values (<50 A/cm^2 and <10^{17}), as shown in Ref. 51. Figure 8a and b plots the aforementioned dependencies. Figure 8a illustrates the dependence of η_{m}, η_{l}, and η_{r} on i. Even at very low current densities (around 1 A/cm^2), it is observed that the diffusion components of the total current (η_{l} and η_{r}) have a higher contribution than the recombination one (η_{m}), as already reported for these current densities.[47,52] η_{m} diminishes as i increases, following a square-like law. This dependence is expected, as $i_{\mathrm{m}} \propto \bar{C}_{\mathrm{SS}} \propto i^{1/2}$ and $\eta_{\mathrm{m}} = i_{\mathrm{m}}/i$.[47] On the other hand, η_{r} and η_{l} maintain a slight dependence on i. This behavior is in accordance with the observed results in Fig. 7, which demonstrates as the P-buffer layer modulates $C_{\mathrm{SS}}(y_{\mathrm{p}})$.[47] Figure 8b reports that γ_{l} and γ_{r} slightly diminish with i following a powerlike law. At first sight, there is no strong dependence of γ_{l} and γ_{r} on i for the selected biasing conditions.

Downloaded 11 May 2010 to 205.161.180.253. Redistribution subject to ECS license or copyright; see http://www.ecsdl.org/terms_use.jsp

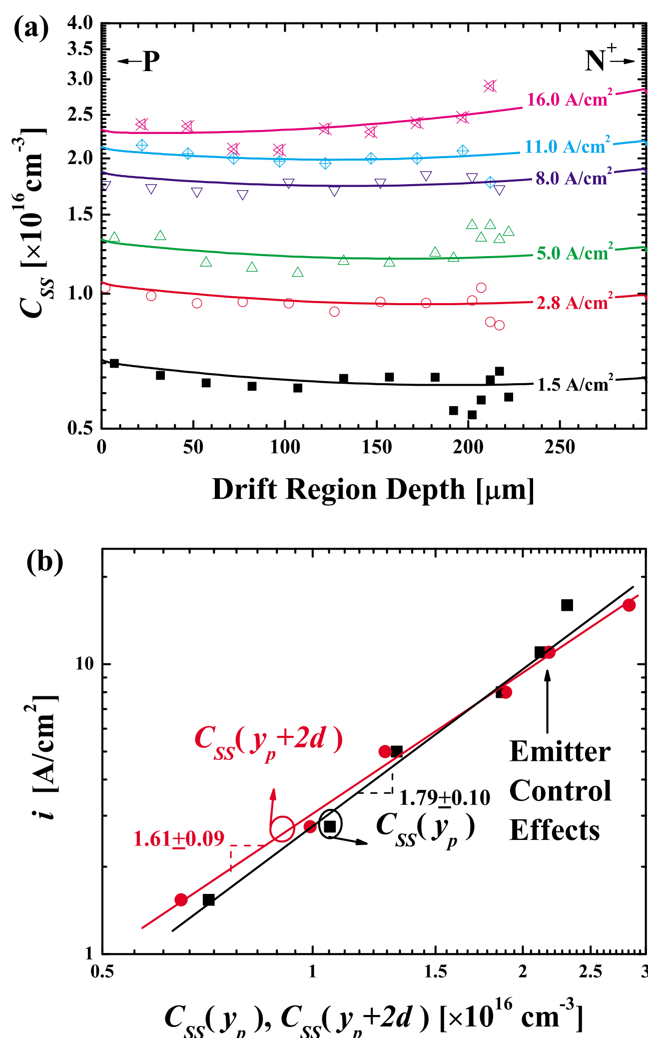

Figure 7. (Color online) (a) Comparison between the measured excess carrier concentration profiles and the results inferred from fitting Eq. 8 to experiment at several current densities. (b) Measured dependence of the current density on $C_{SS}(y_p)$ (red dot points) and $C_{SS}(y_p + 2d)$ (black square points) and its corresponding trend lines.

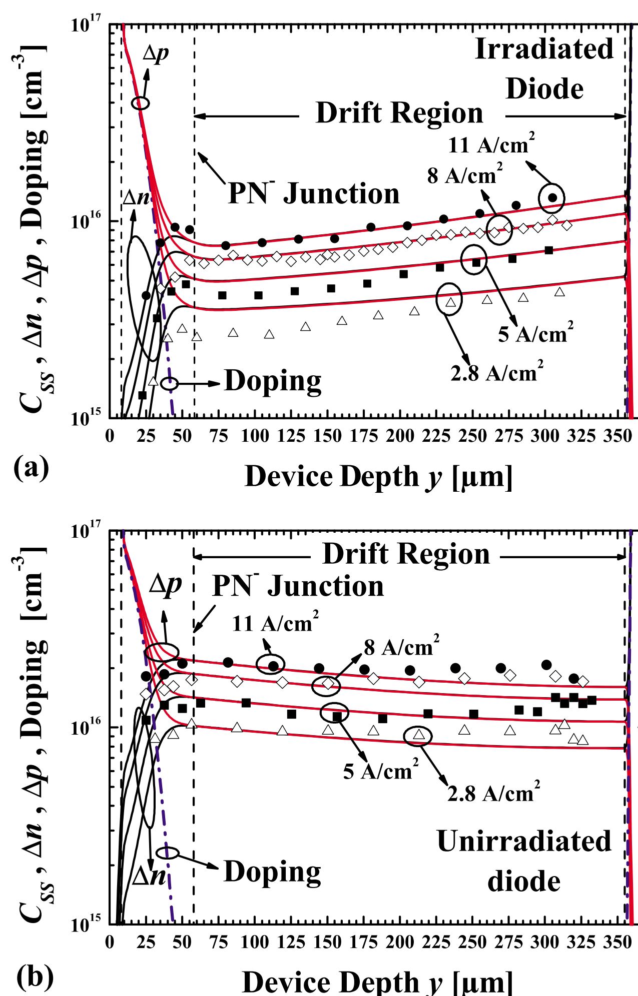

Figure 9. (Color online) Comparison of the excess carrier concentration in the drift region between measurements (points) and simulation results (solid lines) at current densities of 2.8 (white triangles), 5 (black squares), 8 (white diamonds), and 11 (black dots) (A/cm^2) for both diodes: (a) irradiated and (b) unirradiated. From simulation results, the excess carrier concentrations of holes (red solid lines, Δp) and electrons (black solid lines, Δn) are also shown, as well as the doping profile (blue dot-dashed line).

Emitter control and local lifetime tailoring effects on excess carrier concentration.— Due to the lack of analytical models describing the diode forward-bias behavior when ion irradiation was performed, physical device simulations were carried out using the software package Sentaurus device, TCAD.[31] The measured parameters for the lifetime dependence on the doping level were used in the performed simulation. Concerning the irradiated diodes, the deep levels E4 and E1 were considered. From the measurements of high level lifetime profiles, we extracted $f(y)$ and we considered that the same profile $f(y)$ (with $r_p = 60$ μm) applies for both deep levels, but with a different defect concentration peak $N_{t,i}$ (weighting factor). Each $N_{t,i}$ has been modified to obtain the lifetime profile extracted from the irradiated diode. The capture coefficients for the SRH model have been taken from Refs. 28 and 37. In these simulations, the recombination on the polished walls of the devices has not been taken into account. Although this effect is mitigated by the polishing process, C experiences slight changes inside the device that affect the simulation results less than an order of magnitude (as previously demonstrated). Thus, as a first approximation, simulation results provide the trends and the order of magnitude of the excess carrier concentration inside the drift region.

Figure 9a and b illustrates the dependence of C_{SS} profiles on the current density for the irradiated and unirradiated diodes, respectively. In this graph, the experimental (points) and simulation (solid lines) results are compared at several current densities representative

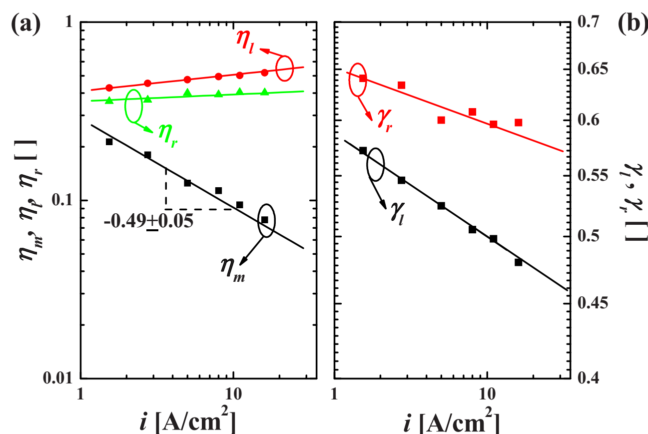

Figure 8. (Color online) (a) Observed dependence of the diffusion and recombination contribution to the total current i. (b) Dependence of PN⁻ and N⁻N⁺ junction injection efficiency on the current density.

Downloaded 11 May 2010 to 205.161.180.253. Redistribution subject to ECS license or copyright; see http://www.ecsdl.org/terms_use.jsp

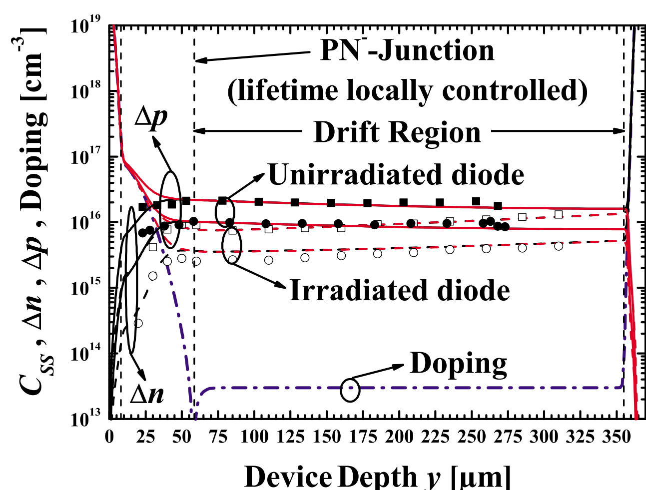

Figure 10. (Color online) Comparison of the excess carrier concentration profiles between experiment (points) and simulation results (solid and dashed lines) for the unirradiated (black symbol) and irradiated diodes (white symbol) at two current densities: 2.8 A/cm^2 (square points, dashed lines) and 11 A/cm^2 (dot points, solid lines). Hole (red solid and dashed lines) and electron (black solid and dashed lines) carrier excess concentrations ($\Delta p, \Delta n$) are also represented, as well as the doping profile (blue dot-dashed line).

of the nonemitter-control regime (2.8, 5, 8, and 11 A/cm^2). In addition, the background doping profile (blue dot-dashed line) is also shown for a better comprehension of the experimental results. In this figure, C_{SS} increases with the current density in both cases, maintaining its profile shape. It can also be observed that the excess carrier concentrations of electrons (Δn, black solid line) and holes (Δp, red solid line) reach the same level along the drift region for both devices (high injection condition). By contrast, Δp and Δn are very different outside this region. Depending on the difference between the excess carrier and doping concentrations, Δn and Δp either increase following the doping profile (majority carrier case) or rapidly decrease to very low concentrations (minority carrier case). It is detected by FCA measurements that C_{SS} slightly overcomes the doping level at the P-buffer anode.

From the comparison between simulation and experiment, they qualitatively agree. As observed in Fig. 9a, the differences between experiment and simulation increase when the current density decreases. Nonetheless, the higher discrepancies between experiment and simulation are observed in the unirradiated diode when C_{SS} is measured closer to the cathode side. As Fig. 9b shows, the experimental points deviate from the simulation results. This may be due to the error introduced by the diode preparation process (within 14% deviation) as previously estimated, but this fact does not affect the interpretation of the results when both devices are compared.

Figure 10 graphically depicts the ion-irradiation modulation on C_{SS} at two current densities, 2.8 A/cm^2 (square points, dashed lines) and 11 A/cm^2 (dot points, solid lines), by comparing experimental (points) and simulation (solid and dashed lines) results for both diodes (unirradiated experimental results in black and irradiated experimental results in white). In addition, the background doping profile (blue dot-dashed line) is also included for a better comprehension. The main difference between both devices stems from the behavior of Δn and Δp in the drift region. In comparison with the unirradiated case, the defects created at the ion penetration range induce a decrease in C_{SS} along the drift region, as $C_{SS}(y_p)$ is reduced by the carrier recombination. As Fig. 10 shows, this effect is experimentally observed, obtaining a good agreement with simulation results. This behavior is due to an increase in $i_m(y_p)$, which induces a decrease in $i_n(y_p)$. This can be demonstrated from the measurements by comparing the η_m and η_l before (i.e., η_m^{unir} and η_l^{unir}) and after (i.e., η_m^{ir} and η_l^{ir}) the device irradiation, expecting to find $\eta_m^{ir} > \eta_m^{unir}$ and $\eta_l^{ir} < \eta_l^{unir}$. This can be derived considering that in the irradiated diode, the recombination current $i_{m,ir}$ corresponds to[47]

$$i_{m,ir} = q\int_{y_p+2d}^{y_p} dy \frac{C_{SS,ir}(y)}{\tau_{HL,bulk}^{ir}(y)} \qquad [25]$$

where $C_{SS,ir}(y)$ is the $C_{SS}(y)$ for the irradiated diode. Taking Eq. 8 and supposing $\{a + b/[1 + (N/N_{ref})]\} \approx 1$ because $N \ll N_{ref}$ in the drift region, as previously demonstrated, the mean value of excess carrier concentration stored in the drift region of the irradiated diode ($\bar{C}_{SS,ir}$) is

$$\bar{C}_{SS,ir} = \frac{\tau_0 i \eta_m^{ir}}{2dq} - \frac{\tau_0}{2d\tau_{ir}}\int_{y_p+2d}^{y_p} dy[C_{SS,ir}(y)f(y)] \qquad [26]$$

Determining both η_m^{ir} from Eq. 26 and η_m^{unir} from Eq. 16, one may infer that i_m is changed by the irradiation process as follows

$$\eta_m^{ir} - \eta_m^{unir} = \frac{q}{i\tau_{ir}}\int_{y_p+2d}^{y_p} dy[C_{SS,ir}(y)f(y)] - \frac{q2d}{\tau_0 i}(\bar{C}_{SS,unir} - \bar{C}_{SS,ir}) \qquad [27]$$

where $\bar{C}_{SS,unir}$ corresponds to the C_{SS} value averaged within the diode drift region, calculated as defined in Eq. 16. By assuming that the ion irradiation does not affect the diffusion current component at the N^-N^+ junction (i.e., η_r), Eq. 27 may be rewritten as

$$\eta_l^{ir} - \eta_l^{unir} = -\frac{q}{i\tau_{ir}}\int_{y_p+2d}^{y_p} dy[C_{SS,ir}(y)f(y)] + \frac{q2d}{\tau_0 i}(\bar{C}_{SS,unir} - \bar{C}_{SS,ir}) \qquad [28]$$

Equations 27 and 28 verify $\eta_m^{ir} - \eta_m^{unir} = -(\eta_l^{ir} - \eta_l^{unir})$ and depict two competing mechanisms, which differently contribute to the diffusion current at the PN^- junction. The locally induced defects increase the current recombination component, diminishing the diffusion one, whereas $\bar{C}_{SS,unir} - \bar{C}_{SS,ir}$ increases the gradient of the carrier concentration at the PN^- junction, provoking the opposite effect. From the design point of view, it is required that the defects' term becomes more important than the reduction in excess carrier concentration. In such an optimal situation, the injection efficiency γ_l of the PN^- junction increases. To check whether the behavior theoretically described corresponds to the observed one on the analyzed diodes, Eq. 27 has been evaluated using the experimental results. We obtain that $\eta_m^{ir} - \eta_m^{unir}$ are 0.14 and 0.20 for $i = 2.8$ A/cm^2 and $i = 11$ A/cm^2, respectively. Therefore, the previous assumptions $\eta_m^{ir} > \eta_m^{unir}$ and $\eta_l^{ir} < \eta_l^{unir}$ are corroborated from the experimental results. Notice that although Eq. 27 and 28 are averaged results along the drift region, their predictions are valid because the local irradiation directly actuate on the efficiency of the PN^- junction, changing the rest of the other parameters within the device drift region.

One may infer from Fig. 10 and 7a that emitter-control techniques are very effective for medium and high current densities but not efficient enough for the operation at very low current densities during a very fast recovery when a snappy recovery can occur and an undesired electromagnetic interference or even a failure can take place.[1] From Eq. 18, it is possible to estimate which is the dependence of the parameter k after irradiation (k_{ir}) on the unirradiated one (k_{unir}) by substituting η_l^{ir} in Eq. 18 after its extraction from Eq. 28. One may see that from the previous results, k_{ir} is related to k_{unir} as

Downloaded 11 May 2010 to 205.161.180.253. Redistribution subject to ECS license or copyright; see http://www.ecsdl.org/terms_use.jsp

$$k_{ir} = k_{unir}\sqrt{1 - \frac{q}{\tau_{ir} i \eta_l^{unir}}\int_{y_p+2d}^{y_p} dy[C_{ir}(y)f(y)] + \frac{q2d}{\tau_0 i \eta_l^{unir}}(\bar{C}_{SS,unir} - \bar{C}_{SS,ir})} \quad [29]$$

As may be inferred from Eq. 29, the ion-irradiation process improves the diode response for low current densities because the condition $k < 1$ can be achieved by (*i*) an appropriate irradiation dose, (*ii*) a sufficiently low doping concentration at the position of the defect peak (ion range), and (*iii*) using both the irradiation and annealing techniques, giving at least one suitable deep level within the bandgap, which controls the low level lifetime. In our case, it is the divacancy $V_0^{(-/0)}$.

As the current density i increases, the recombination current in the drift region diminishes, whereas the diffusion current at both junctions increases.[47] In these current ranges, the excess carrier profile is totally fixed by the emitter-control mechanisms as it is pinned to the doping profile. Therefore, the combination of emitter and lifetime control strategies is the best choice to obtain an optimum excess carrier profile from low to high current densities in a fast-recovery diode.

Conclusions

The excess carrier control mechanisms are measured on fast-recovery diodes working at low current densities when local irradiation is performed. For this purpose, the excess carrier concentration and its lifetime profile are measured in irradiated and unirradiated diodes. From their comparison, it is clearly demonstrated how the excess carrier concentration, jointly with the excess carrier lifetime, is modified by emitter or lifetime engineering approaches. Such measurements have been performed biasing the devices at low current density levels during short pulses (84 μs) to avoid the self-heating effects. From lifetime measurements, it has been possible to extract by simple analytical models the lifetime dependence on the doping level, the defect profile waveform, and the ion-irradiation effect on the lifetime profile. The emitter control by a buffer layer has been studied using an analytical model to highlight its behavior at low current densities. Moreover, the measured excess carrier concentration in both diodes has been compared with simulation results. The simulations have been calibrated by the lifetime measurements performed in both devices to achieve a good agreement between experiment and simulation. As a result, it has been shown how the irradiation can improve the excess carrier distribution for softer fast-recovery diodes at low current densities. A valuable analysis of the lifetime and carrier concentration can be performed by analytical modeling and physical simulation, provided that an accurate parameter identification is available from experiment.

Acknowledgment

This work has been partially supported by the "Consejo Superior de Investigaciones Científicas" (CSIC) (under contract "Junta para la Ampliación de Estudios," JAE-Doc), the Spanish Ministry of Science and Innovation (research programs: THERMOS TEC2008-05577 and RUE CSD2009-00046), and the Ministry of Education, Youth and Sports of the Czech Republic (research program no. MSM 6840770017). The authors acknowledge H. von Kiedrowski (PDI Berlin, Germany) for polishing the samples, Polovodiče a. s. (Prague) for providing the samples, and T. Schumann (FZR Dresden, Germany) for irradiating the diodes.

Centro Nacional de Microelectrónica assisted in meeting the publication costs of this article.

References

1. M. T. Rahimo and N. Y. A. Shammas, *IEEE Trans. Ind. Appl.*, **37**, 661 (2001).
2. A. Porst, F. Auerbach, H. Brunner, G. Deboy, and F. Hille, in *Proceedings of ISPSD*, Weimar, Germany, p. 213 (1997).
3. J. Lutz, in *Proceedings of EPE*, Trondheim, Norway, p. 1502 (1997).
4. M. Rahimo and A. Kopta, in *Proceedings of ISPSD*, Santa Barbara, USA, p. 83 (2005).
5. J. Lutz, R. Baburske, M. Chen, B. Heinze, M. Domeij, H.-P. Felsl, and H.-J. Schulze, *IEEE Trans. Electron Devices*, **56**, 2825 (2009).
6. J. Vobecký, in *Proceedings of ASDAM*, Smolenice Castle, Slovakia, p. 21 (2000).
7. R. Siminiec, F.-J. Niedernostheide, H.-J. Schulze, W. Südkamp, U. Kellner-Werdehausen, and J. Lutz, *J. Electrochem. Soc.*, **153**, G108 (2006).
8. P. Hazdra, J. Vobecký, and K. Brand, *Nucl. Instrum. Methods Phys. Res. B*, **186**, 414 (2002).
9. P. Hazdra, J. Vobecký, H. Dorschner, and K. Brand, *Microelectron. J.*, **35**, 249 (2004).
10. J. Vobecký, P. Hazdra, J. Voves, and F. Spurný, in *Proceedings of ISPSD*, Davos, Switzerland, p. 265 (1994).
11. N. Keskitalo, A. Hallén, F. Masszi, and J. Olsson, *Solid-State Electron.*, **39**, 1087 (1996).
12. O. Humbel, N. Galster, T. Dalibor, T. Wikström, F. D. Bauer, and W. Fichtner, *IEEE Trans. Power Electron.*, **18**, 23 (2003).
13. T. T. Mnatsakanov, A. E. Schlögl, L. I. Pomortseva, and D. Schröder, *Solid-State Electron.*, **43**, 1703 (1999).
14. S. R. Lederhandler and L. J. Giacoletto, in *Proc. IRE*, **43**, 477 (1955).
15. X. Perpiñà, X. Jordà, N. Mestres, M. Vellvehi, P. Godignon, J. Millán, and H. von Kiedrowski, *Meas. Sci. Technol.*, **15**, 1011 (2004).
16. M. Rosling, H. Bleichner, and E. Nordlander, in *Proceedings of EPE-MADEP*, Firenze, Italy, p. 59 (1991).
17. F. Hille, L. Hoffmann, H.-J. Schulze, and G. Wachutka, in *Proceedings of ISPSD*, Toulouse, France, p. 299 (2000).
18. R. Thalhammer, Ph.D. Thesis, Fakultät der Elektrotechnik und Informationstechnik, Technishe Universität München, Munich (2000).
19. L. W. Davies, *Proc. IEEE*, **51**, 1637 (1963).
20. H. Benda and E. Spenke, *Proc. IEEE*, **55**, 1331 (1967).
21. W. Shockley and W. T. Read, *Phys. Rev.*, **87**, 835 (1952).
22. J. Vobecký, P. Hazdra, and V. Záhlava, *Microelectron. J.*, **30**, 513 (1999).
23. H. Bleichner, M. Rosling, J. Vobecky, M. Lundqvist, and E. Nordlander, in *Proceedings of ISPSD*, Tokyo, Japan, p. 246 (1990).
24. M. Rosling, H. Bleichner, M. Lundqvist, and E. Nordlander, *Solid-State Electron.*, **35**, 1223 (1992).
25. X. Perpiñà, X. Jordà, M. Vellvehi, J. Millán, and N. Mestres, *Rev. Sci. Instrum.*, **76**, 025106 (2005).
26. A. E. Schlögl, Ph.D. Thesis, Fakultät der Elektrotechnik und Informationstechnik, Technishe Universität München, Munich (1999).
27. H.-J. Schulze, A. Frohnmeyer, F.-J. Niedernostheide, F. Hille, P. Tütto, T. Pavelka, and G. Wachutka, *J. Electrochem. Soc.*, **148**, G655 (2001).
28. P. Jonsson, H. Bleichner, M. Isberg, and E. Nordlander, *J. Appl. Phys.*, **81**, 2256 (1997).
29. H. Schlangenotto and H. Maeder, *IEEE Trans. Electron Devices*, **26**, 191 (1979).
30. W. Gerlach, H. Schlangenotto, and H. Maeder, *Phys. Status Solidi A*, **13**, 277 (1972).
31. Synopsys, Sentaurus Device User Guide, Version A-2008.09 (2008).
32. D. K. Schroder, *IEEE Trans. Electron Devices*, **44**, 160 (1997).
33. K. L. Luke and L.-J. Cheng, *J. Appl. Phys.*, **61**, 2282 (1987).
34. Z. G. Ling, P. K. Ajmera, and G. S. Kousik, *J. Appl. Phys.*, **75**, 2718 (1994).
35. S. Sumie, F. Ojima, K. Yamashita, K. Iba, and H. Hashizume, *J. Electrochem. Soc.*, **152**, G99 (2005).
36. J. F. Ziegler and J. P. Biersack, SRIM2000.39, Stopping and Range of Ions in Matter (2000).
37. A. Hallén and N. Keskitalo, *J. Appl. Phys.*, **79**, 3906 (1996).
38. Synopsis, Sentaurus Device User Guide, p. 293 (2008).
39. J. G. Fossum and D. S. Lee, *Solid-State Electron.*, **25**, 741 (1982).
40. J. Vobecký, P. Hazdra, O. Humbel, and N. Galster, *Microelectron. Reliab.*, **40**, 427 (2000).
41. H. Bleichner, P. Johnsson, N. Keskitalo, and E. Nordlander, *J. Appl. Phys.*, **79**, 9142 (1996).
42. B. J. Baliga, *Modern Power Devices*, p. 196, Wiley-Interscience, Singapore (1987).
43. J. P. Spratt, E. A. Burke, J. C. Pickel, and R. E. Leadon, *IEEE Trans. Nucl. Sci.*, **48**, 2136 (2001).
44. J. Vobecký, P. Hazdra, and V. Záhlava, *Microelectron. Reliab.*, **43**, 537 (2003).
45. A. Hallén and N. Keskitalo, *Nucl. Instrum. Methods Phys. Res. B*, **186**, 344 (2002).
46. P. Hazdra, J. Rubeš, and J. Vobecký, *Nucl. Instrum. Methods Phys. Res. B*, **159**, 207 (1999).
47. A. Herlet, *Solid-State Electron.*, **11**, 717 (1968).
48. G. Baccarani and P. Ostoja, *Solid-State Electron.*, **18**, 579 (1975).
49. D. M. Caughey and R. E. Thomas, *Proc. IEEE*, **55**, 2192 (1967).
50. M. Rosling, H. Bleichner, P. Jonson, and E. Nordlander, *J. Appl. Phys.*, **76**, 2855 (1994).
51. F. Berz, R. W. Cooper, and S. Fagg, *Solid-State Electron.*, **22**, 293 (1979).
52. S. K. Ghandi, *Semiconductor Power Devices*, p. 93, Wiley-Interscience, New York (1977).

Downloaded 11 May 2010 to 205.161.180.253. Redistribution subject to ECS license or copyright; see http://www.ecsdl.org/terms_use.jsp